Journal of Materials Chemistry A

ROYAL SOCIETY OF CHEMISTRY

PAPER

View Article Online
View Journal | View Issue

Cite this: J. Mater. Chem. A, 2024, 12, 3434

Alcohol-based adsorption heat pumps using hydrophobic metal–organic frameworks†

R. M. Madero-Castro,‡[a] A. Luna-Triguero, ‡[bc] C. González-Galán,[a] José Manuel Vicent-Luna *[cd] and Sofía Calero *[cd]

The building climatization and its influence on energy consumption have consequences on the environment due to the emission of greenhouse gases. Improving the efficiency of this sector is essential to reduce the effect on climate change. In recent years, the interest in porous materials in applications such as heat pumps has increased because of their promising potential. To assess the performance of adsorption heat pumps and cooling systems, here we discuss a multistep approach based on the processing of adsorption data combined with a thermodynamic model. The process provides properties of interest, such as the coefficient of performance, the working capacity, the specific heat or cooling effect, or the released heat upon adsorption and desorption cycles, and it also has the advantage of identifying the optimal conditions for each adsorbent–fluid pair. To test this method, we select several metal-organic frameworks that differ in topology, chemical composition, and pore size, which we validate with available experiments. Adsorption equilibrium curves were calculated using molecular simulations to describe the adsorption mechanisms of methanol and ethanol as working fluids in the selected adsorbents. Then, using a thermodynamic model we calculate the energetic properties combined with iterative algorithms that simultaneously vary all the required working conditions. We discuss the strong influence of operating temperatures on the performance of heat pump devices. Our findings point to the highly hydrophobic metal azolate framework MAF-6 as a very good candidate for heating and cooling applications for its high working capacity and excellent energy efficiency.

Received 31st August 2023
Accepted 8th December 2023

DOI: 10.1039/d3ta05258c

rsc.li/materials-a

1 Introduction

The demand for energy efficiency has increased in the last two decades.[1,2] Forecasts manifest that this growth will continue due to global warming.[2,3] Consequently, the emission of greenhouse gasses into the atmosphere will be higher, producing a feedback process.[4–6] Improving efficiency in this sector and reducing greenhouse gasses emissions are critical aspects in mitigating climate change.[7–10] Traditional heating systems such as electric or gas heaters offer low performance.[11] They are based on the Joule effect or on the specific heat of the substances to be burned, respectively, so that the heat supplied for the heating system is equal to the energy used. It is essential to develop advanced heating devices that take advantage of outside heat to increase performance. For example, heating devices such as solar collectors, which use solar energy to warm water or air, are eco-friendly options.[12–14] The main problem with solar systems is that weather acts as a restrictive factor.[15]

Heat pumps are a promising alternative since they take heat from the surroundings, reducing the total energy consumption of the heating system.[16] These systems are efficient and a sustainable alternative to conventional methods, increasing the performance and decreasing the amount of greenhouse gasses released into the atmosphere. Traditional heat pumps are based on the compression/decompression of a working fluid, with hydrofluorocarbons (such as HFC-134a or HFC-125) being the most used at the industrial level.[17,18] The main drawback of these devices is that they use greenhouse gasses[19] that need to be reduced according to the Montreal Protocol.[19] In this context adsorption-based heat pumps (AHPs) and adsorption cooling systems (ACSs) using porous materials, can be

[a]Department of Physical, Chemical, and Natural Systems, Universidad Pablo de Olavide, Ctra. Utrera km. 1, ES-41013, Seville, Spain
[b]Department of Mechanical Engineering, Eindhoven University of Technology, 5600 MB, Eindhoven, The Netherlands
[c]Eindhoven Institute for Renewable Energy Systems (EIRES), Eindhoven University of Technology, Eindhoven 5600 MB, The Netherlands
[d]Department of Applied Physics, Materials Simulation & Modelling, Eindhoven University of Technology, 5600 MB, Eindhoven, The Netherlands. E-mail: s.calero@tue.nl; j.vicent.luna@tue.nl

† Electronic supplementary information (ESI) available: Structural properties of the adsorbents (Fig. S1 and Table S1), additional details of the models and adsorption conditions (Fig. S2 and Table S2), structural and energetic properties of the adsorbates in confinement (Fig. S3 and S4), comparison between computed and predicted isotherms (Fig. S5 and S6), heat energy transferred to the condenser (Fig. S7–S10), deliverable capacity (Fig. S11), and specific cooling and heating effect of methanol and ethanol (Fig. S12 and S13). See DOI: https://doi.org/10.1039/d3ta05258c

‡ These authors contributed equally to this work.

alternatives. The operation mechanism of the AHP and ACS devices is based on the adsorption and evaporation of a refrigerant. These devices follow the assumption that reversible adsorption (desorption) is an exothermic (endothermic) process.[20]

In recent years, AHPs and ACSs made with porous materials such as activated carbons,[14,21–29] zeolites,[29–37] and metal–organic frameworks (MOFs)[29,38–43] have shown promising performance and benefits in cost and versatility. Pal *et al.*[44] studied the production of highly porous carbons from vegetable waste for heat pump applications. Works reported by de Lange *et al.*,[45] Li *et al.*,[46] Erdős *et al.*,[47] or Jeremias *et al.*,[48] among others, studied a variety of MOFs with methanol and ethanol as working fluids for adsorption-driven heat pump and chiller applications. Kayal *et al.*[49] studied the water-AQSOA zeolite working pair to create adsorption chillers, concluding that these zeolites are also suitable for this purpose. One of the most challenging parts of designing AHPs is the selection of the working pair. It is desirable to work with environmentally friendly fluids with a high enthalpy of vaporization. However, the large amount of synthesized porous adsorbents makes it difficult to assess the performance of each working pair experimentally. Computationally, testing several operating conditions for the selection of the optimal range for a given pair is also very expensive. The number of synthesized MOFs is large and continuously growing.[50] Their high versatility in terms of composition and pore size makes them good candidates to operate under different conditions. In-depth knowledge of the adsorbent–fluid interactions makes it possible to choose the most suitable pair for the given working conditions. In general, MOFs exhibit higher adsorption capacity than zeolites or other porous materials, a fundamental aspect of increasing the heat transfer between adsorption/desorption cycles. In this work, we have selected ZIF-8, ZIF-71, ZIF-90, MIL-140C, and MAF-6 as adsorbents. Four of these MOFs exhibit large pore size (>11 Å), which is desired for a stepwise isotherm. The exception is MIL-140C, with a pore size lower than 6 Å, which we include for comparison. These MOFs have been successfully tested for the adsorption of methanol and ethanol.[45,51,52] We use these experimental data to validate our models.

The selection of the refrigerant for an adsorption energy storage device is as important as the selection of the adsorbent, because the synergy between the adsorbent and fluid working pairs is a critical aspect for achieving maximum performance. Working fluids such as small alcohols has been proposed as alternatives to conventional refrigerants,[30,53] and water.[53,54] Water is an excellent candidate due to its high enthalpy of vaporization and zero toxicity to humans, but as a downside, water can affect MOF stability.[55] Ammonia is also an excellent working fluid with a low melting point (−40 °C) and slightly lower enthalpy of vaporization than water. However, ammonia is a toxic compound that should be used carefully. In the search for other working fluids for AHPs and ACSs, light alcohols have become a possible alternative.[45,56] Highly hydrophobic materials cannot adsorb/desorb water under realistic pressure/temperature conditions.[57–60] However, these adsorbents can capture and release methanol and ethanol within the range of operating conditions. de Lange *et al.*[45] summarized the main differences between replacing water (the most common working fluid in MOFs) with ethanol and methanol. These are, among others (1) a decrease in the onset pressure of methanol and ethanol compared to that of water, (2) a smaller hysteresis loop for large pore materials (below 3.4 nm), (3) lower energy release per cycle, but heat and mass transfer may be improved, and (4) in general, MOFs seem to be more stable upon alcohol adsorption than upon water adsorption. These facts make light alcohols a promising alternative to water and other common refrigerants used in industry. Another important aspect is the reduced global warming potential (GWP) of small alcohols compared to traditional working fluids. The ethanol GWP fluctuates between 0.31 and 5.55 depending on the production path[61] compared to the 1120–3500 GWP for HFC-based refrigerants, *i.e.* HFC-134a and HFC-125. Hence, in addition to the previous discussion, the relatively low cost, high heat capacities, and low melting points make methanol and ethanol good candidates as working fluids for AHP/ACS applications.

The large amount of synthesized structures makes the assessment of the performance of each working pair challenging from an experimental point of view. Several studies focused on strategies to analyze the performance of the alcohol-adsorbent using computational screenings. Erdős *et al.*[47] designed a screening process for methanol and ethanol for about 3000 adsorbents. The most promising structures were selected based on the maximum working capacity obtained in consecutive relative values of pressure defined by the authors. A computational screening and selection based on the coefficient of performance (COP) for cooling applications was reported by Li *et al.*[46] They systematically rejected structures that perform below the imposed limit of 0.8. The significant number of samples made an in-depth study challenging under suitable operating conditions for each system, which led to qualitative-based interpretations. To speed up the selection process, they performed relatively short GCMC simulations (4×10^4 cycles), only running more cycles for the promising structures. This approach aimed to obtain high-performance structures. However, short simulations in the first step can also lead to the rejection of viable materials. It has been previously demonstrated that materials with big pores and hydrophobic structures need more MC cycles to reach equilibrium.[54] Following a similar approach, another recent computational screening by the same authors[62] analyzed the performance of COF–ethanol working pairs for heating, cooling, and ice-making applications. As before, they performed short GCMC simulations that could disregard promising candidates. Each adsorbent–fluid pair and its range of operating conditions should be analysed carefully. This is because any small change could imply considerable deviation in the predicted application of heating and cooling systems. In this regard, Xia *et al.*[63] went a step further by varying the working conditions and the effect on the cooling/heating performance of COF-5/ethanol and several MOF/ethanol working pairs. In addition, a few theoretical approaches have been proposed to study the performance of AHP devices based on hypothetical and idealized adsorbents. Bagheri and Schiffres[64] proposed a method for finding the ideal step location

as a function of the operating conditions and applied it to test systems based on 13X-water and UIO-66-water working pairs. Jiang *et al.*[65] proposed a framework based on the ideal adsorption isotherm behavior to obtain the thermodynamic limits of an AHP system. The authors applied this methodology to MOF-801-water and 13X-water working pairs, analyzing the role of the operating conditions. Later on, Li *et al.*,[66] went a step further and proposed a method and set the relationships between the optimal step location and the AHP performance under different conditions. These theoretical approaches highlight the importance of considering the operating conditions for the analysis of the performance of AHP systems and agree that stepwise isotherms are desired for efficient AHP applications.

Here, we propose a novel approach to assess the coefficient of performance or other thermodynamic quantities, such as the heat released during the adsorption process. We apply this method to investigate MOF-methanol/ethanol working pairs and rely on adsorption data and the consecutive application of mathematical and thermodynamic models. We have selected hydrophobic MOFs with large pore cavities that exhibit stepwise isotherms for small polar molecules such as light alcohols. The advantage of this methodology is that it can be applied to either experimental or computational data sets and is also extensible to other working fluids. Another benefit of the analysis proposed here is that we considered a wide range of operating conditions, proving that setting the operating temperatures could lead to a significant loss of information about the performance of the process. In short, an AHP cycle consists of four primary parts: an adsorber containing the adsorbent, a condenser, an evaporator, and an expansion valve. The heat pump operates by driving the adsorbate between the adsorber, condenser, and evaporator. The cycle can be divided in two parts. In the first part, the evaporator vaporizes the fluid, taking heat from a low-temperature source and releasing heat to an intermediate temperature source (adsorption). In the second part, during the condensation of the fluid, the condenser receives heat from a high-temperature source and releases heat to a second intermediate temperature source (desorption). During the cycle, the evaporator, condenser, desorption, and intermediate temperatures play an important role in the performance of the process. Our approach simultaneously screens all these temperatures, providing detailed information on the operation of each MOF–fluid working pair.

With this work, we want to understand the mechanisms that govern the adsorbate–adsorbent pair that enhances the efficiency of the thermodynamic cycle based on the adsorption equilibrium properties of ethanol and methanol in MOFs. We search for optimal conditions for each MOF–alcohol pair, discussing the limitations of setting the values of operating temperatures on the different energetic properties.

2 Methodology

We propose a multistep process as a method to assess the performance of MOFs for heating and cooling applications and as a tool for finding the optimal working conditions for each adsorbent–fluid working pair. This method is tested with five MOFs, namely ZIF-8, ZIF-71, ZIF-90, MIL-140C, and MAF-6, for the adsorption of methanol and ethanol working fluids. The multistep process consists of a combination of molecular simulations, thermodynamical modeling, and in-house algorithms that iteratively analyze the performance of the AHP/ACS process.

2.1 Adsorbents

ZIF-8, ZIF-71, ZIF-90, and MAF-6 are Zn-based zeolitic imidazolate frameworks (ZIFs), and MIL-140C is a Zr-based MOF already used for this type of application.[45] Table S1† summarizes the topology, structural properties, pore volume (V_p), surface area (SA), framework density (ρ), and helium void fraction (HvF) of the selected adsorbents. The table includes the experimental surface area and pore volume for comparison, showing that the computed values follow a similar trend to those for the experimental samples. ZIF-8 (ref. 67) and ZIF-90 (ref. 68) exhibit SOD topology and are formed by Zn metal centers connected to 2-methylimidazole and 2-carboxyaldehyde organic linkers, respectively. The SOD topology is characterized by sodalite central cages interconnected through small windows. ZIF-8 and ZIF-90 have pores in the range of 10.5–11 Å and apertures of 3.5 Å. ZIF-71 (ref. 69) and MAF-6,[60] with RHO topology, are formed by Zn metal centers connected to Zn metal centers connected with 4,5-dichloroimidazole and 2-ethylimidazole organic linkers, respectively. The RHO topology structures are constructed from large central cages interconnected through channels. These two MOFs have similar pore sizes, big cages of about 16.5–17.5 Å and cylindrical channels of 6.5–7 Å. The nature of the organic ligand exerts strong influence on the available pore volume of ZIF-71 and makes MAF-6 the MOF with the largest pore volume. MIL-140C[70] is a five-coordinated Zr-based MOF with a biphenyl-4,4′-dicarboxylic acid linker. The structure has small triangular-shaped channels of about 6 Å that propagate along the *c*-axis. Of the five structures, MIL-140C is the smallest in terms of available pore volume and surface area. Fig. S1† displays the schematic framework connectivity and pore size distribution (PSD). The schematic representation of the ligands can be found in the ESI (Fig. S2†).

2.2 Simulation details

Adsorption capacity as a function of temperature or external pressure was calculated using Monte Carlo (MC) simulations in the grand-canonical ensemble (GCMC) with the RASPA software.[71,72] The MC production run cycles range between 7×10^5 and 2.2×10^6. The number of cycles changes depending on the nature of the system working fluid–adsorbent to ensure that the results fluctuate around an equilibrium value.[54] To this aim, we performed consecutive production runs until the cumulative average values of the adsorbed amount showed an almost constant value. Then, we use statistical ensemble averages to compute the system's properties over the last 5×10^5 MC cycles. The interactions between adsorbates and adsorbents are described with Lennard-Jones and coulombic potentials. We employed Lorentz–Berthelot mixing rules[73] to calculate

Lennard-Jones crossed terms between different atoms, and no tail corrections were applied to the Lennard-Jones potential. We fixed the length of the simulation box so that it always exceeds twice the spherical cut-off of 12 Å. Electrostatic contributions to the energy of the system have been obtained with the Ewald summation method.[74] The flexible pseudo-atom model included in the transferable potentials for phase equilibria (TraPPE) force field[75] was used to describe the alcohol molecules, and it is suitable to describe the adsorption of light alcohols in ZIFs.[76,77]

The structure of the adsorbents is considered rigid during the simulations, placing the framework atoms in their crystallographic positions. We used the reported crystal structures of ZIF-8,[67] ZIF-71,[78] MIL-140C,[70] ZIF-90,[79] and MAF-6.[80] As is common in the case of MOFs, the Lennard-Jones parameters for the adsorbents are taken from DREIDING[81] except for those of the metal atoms taken from UFF.[82] The partial charges of the adsorbents (see Fig. S2 of the ESI†) are calculated using the EQeq method[83] except for that of MAF-6, taken from the previous work of Gutierrez-Sevillano *et al.*[84] Since the interaction between molecules of alcohols *via* hydrogen bonds plays an essential role in the adsorption mechanism,[76] we computed the average number of hydrogen bonds per molecule (nHB) using the methodology described in our previous work.[76]

2.3 Thermodynamic model

The AHP cycle consists of two steps for adsorption (isobaric adsorption and isosteric heating) and two for desorption (isobaric desorption and isosteric cooling), as represented in Fig. 1. The system has different operating condition pairs (p, T) during the cycle, the temperature of the evaporator (T_{ev}), the temperature of the condenser (T_{con}), the temperature of desorption (T_{des}), and intermediate temperatures ($T_{ev} < T_{con} < T_1 < T_2 < T_3 < T_{des}$), and associated pressures. The adsorption and desorption phases of an AHP are characterized by the energy in the different stages: heat taken from the evaporator (Q_{ev}), required energy for desorption or regeneration (Q_{reg}), heat released by the condensed fluid (Q_{con}), and heat released during the adsorption (Q_{ads}) at intermediate temperature. For practical reasons, it is common to assume that T_1, also called the minimum temperature of adsorption (T_{ads}), is equal to T_{con}.

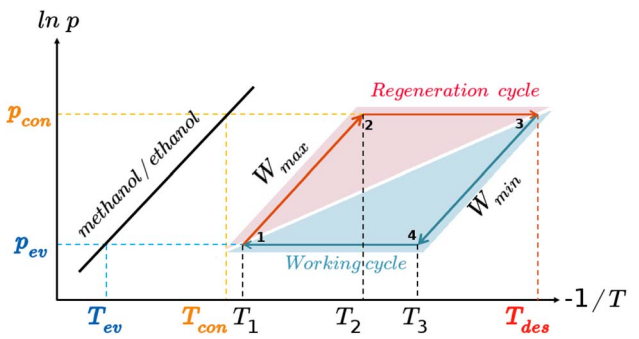

Fig. 1 Isosteric cycle of an AHP, including vapor pressure of alcohol molecules (black line), temperature and pressure of the evaporator (T_{ev}, p_{ev}), and the condenser (T_{con}, p_{con}), desorption temperature (T_{des}), and intermediate cycle temperatures ($T_{(1-3)}$). The working cycle (adsorption) is highlighted in blue and the regeneration cycle (desorption), in red.

The coefficient of performance (COP), used to describe the energetic efficiency, is defined as the ratio between the obtained energy and the input energy. The obtained energy or delivered energy is also defined as the specific heating or cooling effect (SHE or SCE). For heating, the COP is defined as

$$\mathrm{COP_H} = \frac{-(Q_{con} + Q_{ads})}{Q_{reg}} = \frac{\mathrm{SHE}}{Q_{reg}} \quad (1)$$

and for cooling

$$\mathrm{COP_C} = \frac{Q_{ev}}{Q_{reg}} = \frac{\mathrm{SCE}}{Q_{reg}} \quad (2)$$

Q_{con} and Q_{ev} are proportional to the enthalpy of vaporization (ΔH_{vap}), the density of the working fluid (ρ^{wf}) in confinement, and the working capacity (ΔW), which is the difference between the maximum and minimum adsorption isosteres ($W_{max} - W_{min}$). The calculation of the energy needed for regeneration (Q_{reg}) and the energy released during adsorption (Q_{ads}) requires the estimation of the enthalpy of adsorption, ΔH and the enthalpy of vaporization of the working fluid, ΔH_{vap}. The calculation of the enthalpy of adsorption is described below. The enthalpy of vaporization is taken from Majer *et al.*,[85] while the remaining parameters are calculated using models. The equations that govern the AHP process from a thermodynamic perspective are detailed in the literature.[45]

Based on the Dubinin–Polanyi (DP) theory,[86–90] any equilibrium adsorption curve where loading is pressure and temperature dependent, $q(p, T)$, can be reduced to a characteristic curve. The characteristic curve is the relation between the potential of adsorption (A) and the adsorbed specific volume (W) defined as:

$$A = RT\left(\ln\frac{p_0(T)}{p}\right) \quad (3)$$

$$W = \frac{q(p,\ T)}{\rho^{wf}(T)} \quad (4)$$

where p_0 is the vapor pressure of the working fluid, q is the mass adsorbed, and ρ^{wf} is the density of the working fluid in the adsorbed phase. We used the Peng–Robinson equation of state[91] to set the saturation pressure. We calculated the adsorbate density using the Hauer model.[92] This model establishes linear relations between the bulk density and the density inside the pores of the structure. The model was initially developed for water and has been modified to estimate the density of alcohols where $\rho(T_0)$ is the free liquid density taken from experimental data at the reference temperature ($T_0 = 283$ K).[93]

$$\rho^{wf}(T) = \rho(T_0)[1 - \alpha_T(T - T_0)] \quad (5)$$

The coefficient of thermal expansion of the fluid in the adsorbed phase, α_T, is considered constant for each working fluid. α_T has been calculated using the equation

$$\alpha_T = -\frac{1}{\rho(T)}\left(\frac{\partial \rho(T)}{\partial T}\right)_p \quad (6)$$

using the density of the fluid at high pressure, 100 MPa. At $T =$ 300 K, α_T is 8.026 $\times$ 10^{-4} [K^{-1}] for methanol and 7.285 $\times$ 10^{-4} [K^{-1}] for ethanol.

Another interesting fact within the formulation of the DP theory is that it allows us to calculate the adsorption enthalpy from the characteristic curve using numerical techniques.[94] This formulation has been extensively used in the literature for the study of porous adsorbents for energy storage applications.[37,56,89,90,95] The enthalpy of adsorption can be calculated using the enthalpy of vaporization, the adsorption potential, which is the molar free energy of adsorption with opposite sign, and the entropy variation:

$$\Delta H = \Delta H_{vap} + A - T\Delta S \quad (7)$$

The entropy variation term can be calculated from the slope of the characteristic curve as:[90,94]

$$\Delta S = \alpha_T W \left.\frac{\partial A}{\partial W}\right|_T \quad (8)$$

where α_T is calculated through eqn (6).

The DP theory has been questioned because it is based on the postulate that the mechanism for adsorption in micropores is that of pore filling rather than layer-by-layer formation of a film on the walls of the pores, which may describe the adsorbate with fixed characteristic energy and lead to a value of enthalpy of adsorption close to the enthalpy of vaporization of the fluid. In previous studies, we have used this theory to calculate the enthalpy of adsorption of (i) light alcohols in activated carbons with functional groups acting as strong interaction sites for adsorption,[56] (ii) of methanol and water in aluminosilicates by changing the Si/Al ratio giving rise to hydrophilic and hydrophobic adsorbents,[37] and (iii) for water in mesoporous carbons.[96] In these studies, we have demonstrated that the predicted enthalpy of adsorption agrees with the experimental value. Hence, we can conclude that this theory can be applied to structures with and without strong interaction sites, at least if they exhibit large enough pores to allow molecules to nucleate *via* hydrogen bonds, the primary reason for the heat of adsorption converging to values close to the enthalpy of vaporization of the adsorbed fluid. However, further research must be conducted to analyze the applicability of this theory to working pairs of a diverse nature.

2.4 Multistep process

The process is schematically presented in Fig. 2. Step 1 is to obtain the equilibrium adsorption curves, *e.g.*, adsorption isotherms and isobars. This can be done either experimentally or with GCMC simulations. In step 2, the input data are processed according to Dubinin–Polanyi theory using eqn (3) and (4). This leads to a temperature invariant characteristic curve that allows us (i) to predict new adsorption curves under any conditions (step 1) and (ii) to proceed with the thermodynamic analysis of the system.

The application of the DP theory requires inserting preprocessed functions into the algorithm. The most important variables are the density of the fluid in confinement (ρ^{wf}) using eqn (5) and (6), and the saturation pressure (p_0) using the Peng–Robinson equation of state. Once the characteristic curve has

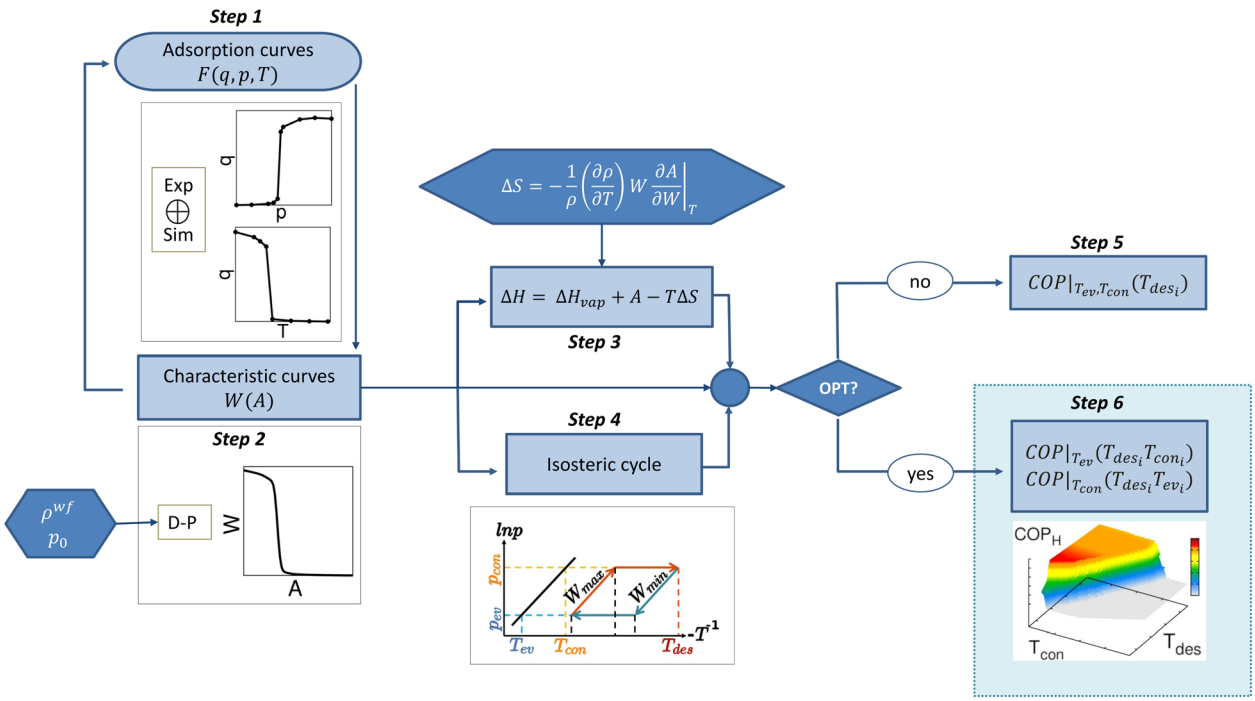

Fig. 2 Schematic algorithm for the multistep process. Each of the steps are described in Section 2.4 of the Methodology section.

been obtained, the process bifurcates. During step 3, we calculate the enthalpy of adsorption of the system using eqn (7), which depends on the enthalpy of evaporation of the fluid, adsorption potential, and entropy. The entropy calculation is pre-processed due to its dependency on the thermal expansion coefficient of the fluid in confinement (eqn (8)). In step 4, the isosteric cycle is calculated, estimating the maximum and minimum capacity isosteres for the given conditions, *i.e.*, setting T_{ev} and T_{con} and the associated pressures. The calculation of COP for either heating or cooling can be done under different conditions (step 5). Without optimization, the temperatures of the evaporator and the condenser are fixed, and therefore, so are the associated pressures. The COP is assessed as a function of the desorption temperature. Step 6 is the optimization step. Here we scan the operating conditions and associated thermodynamic parameters in subsequent loops. The variations of T_{ev}, T_{con}, and T_{des} are carried out simultaneously, with the only condition of $T_{ev} < T_{con} < T_{des}$. After massive data generation, the algorithm computes the COP by setting only one temperature (T_{ev} or T_{con}) and scanning for the optimal conditions. From this step, a 3D plot per fixed variable is obtained, which allows the operating conditions that provide the maximum performance to be chosen. Using the same procedure, we calculated other quantities of interest, such as working capacity, specific heating effect (SHE), specific cooling effect (SCE), and heat released to the condenser (Q_{con}) or the evaporator (Q_{ev}).

3 Results and discussion

We calculated the adsorption isotherms of methanol and ethanol for comparison with reported experimental data for ZIF-8,[45,51] ZIF-71,[51] MIL-140C,[45] ZIF-90,[51] and MAF-6.[52] This first set of calculations (Fig. 3) was used to test the suitability of the force field to reproduce the experimental adsorption of these polar molecules in the selected MOFs. Computed and experimental adsorption isotherms are in line. Discrepancies in the onset pressures of ZIF-90 and ZIF-71 are attributed to the use of a generic force field, which has not been refitted for a particular adsorbent–adsorbate pair. For example, ZIF-90 has exposed oxygen atoms in the ligand, while ZIF-71 has chlorine atoms accessible to the adsorbates. It is expected that alcohol molecules interact through the –OH groups with these electronegative atoms. However, the generic force field is not trained to reproduce these particular interactions and can cause a slight overestimation and underestimation of the onset pressures of ZIF-71 and ZIF-90, respectively. We found larger deviations for the adsorption isotherms of the two alcohols in MIL-140C, overestimating the adsorption capacity of methanol and underestimating the adsorption capacity of ethanol. Based on this, we cannot rule out any flexibility effect of MIL-140C neglected in the simulations. However, the general behavior of all isotherms for the rest of the MOFs is well described by the selected force field, making it suitable for studying the adsorption of alcohols in zeolitic imidazolate frameworks.

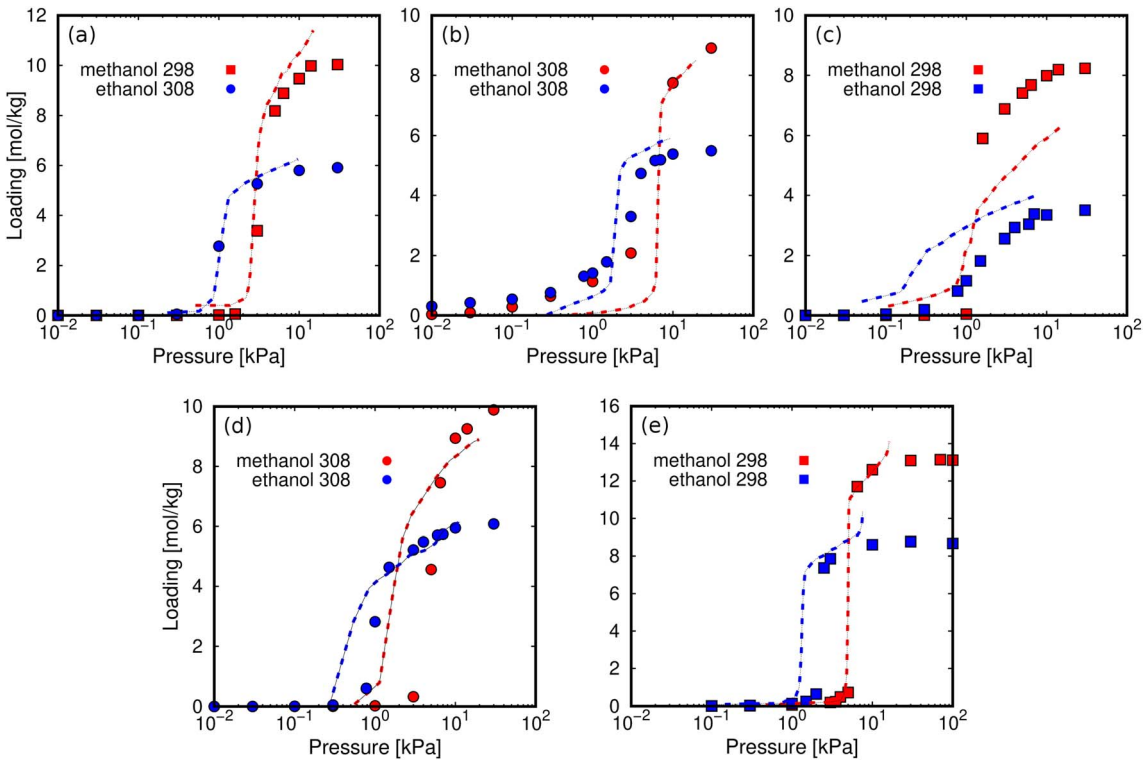

Fig. 3 Computed adsorption isotherms (symbols) of methanol (red) and ethanol (blue) in (a) ZIF-8, (b) ZIF-71, (c) MIL-140C, (d) ZIF-90, and (e) MAF-6 at 298 K (squares) and 308 K (circles). The experimental values (dashed lines) are taken from the literature (ZIF-8,[45,51] ZIF-71,[51] MIL-140C,[45] ZIF-90,[51] and MAF-6 (ref. 52)).

Fig. 4 compares the adsorption characteristics of the working fluids at room temperature. The adsorption isotherms of methanol and ethanol in ZIF-8 and ZIF-90 (Fig. 4a and b), which have SOD topology, show very similar behavior. This can be explained in terms of similar structural properties and composition. The other pair of adsorbents that share RHO topology are ZIF-71 and MAF-6. The presence of chlorine atoms in ZIF-71 has significant effects on the adsorption. Compared to MAF-6, we observe a decrease in the adsorption capacity and a slight attenuation of the abrupt step caused by the presence of accessible chlorine atoms in the pores of ZIF-71, making this adsorbent more hydrophilic than MAF-6. As the most hydrophobic MOF, MAF-6 shows the highest adsorption capacity and higher onset pressures for both adsorbates. MIL-140C shows the lowest ethanol capacity, while the adsorption of methanol is like that obtained in the other MOFs. This is due to a more efficient packing of methanol than ethanol within the small channels of MIL-140C, which is directly related to kinetic diameters, 3.6 and 4.3 Å, respectively.[97]

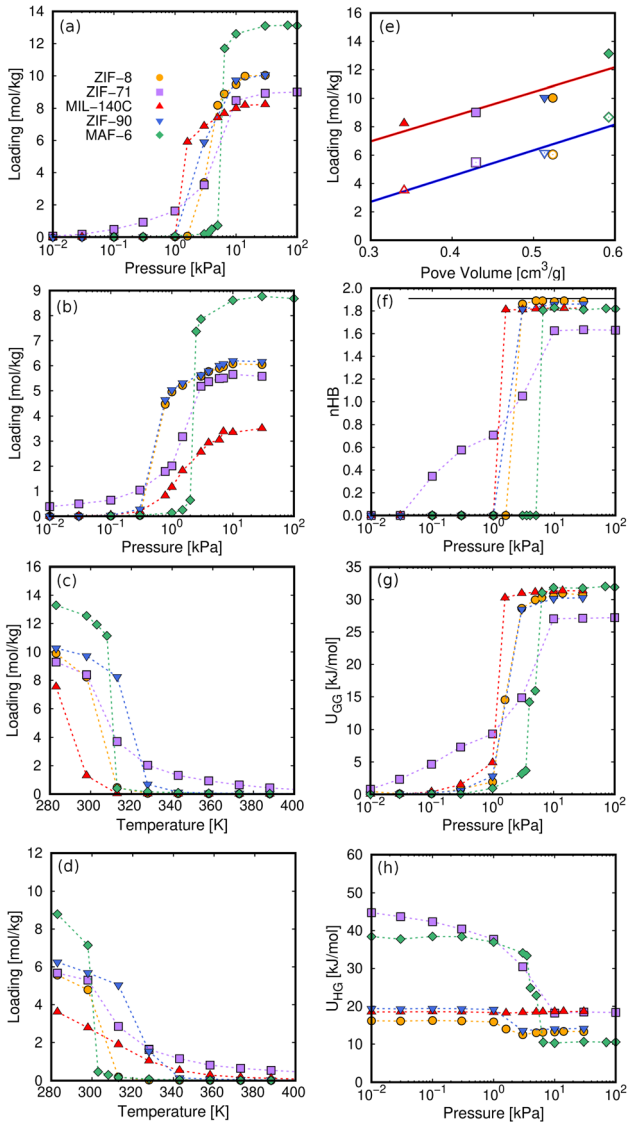

Fig. 4 Adsorption properties of methanol and ethanol in the selected MOFs. Computed adsorption isotherms of (a) methanol and (b) ethanol at 298 K, and adsorption isobars of (c) methanol and (d) ethanol at the selected working pressures shown in Table S2 (ESI†). (e) Saturation capacity of methanol (closed symbols) and ethanol (open symbols) as a function of pore volume. The solid lines in (e) stand for the fitted values to a straight line showing the dependence of loading on the pore volume. (f) nHB, (g) guest–guest interactions, and (h) host–guest interactions of methanol as a function of the pressure. Non-depicted error bars denote fluctuations smaller than the symbol size.

For practical application, it is important to maximize the thermodynamic efficiency of the system.[98] The choice of operating conditions is key in the design of AHP and ACS devices. As shown in Fig. 1, the thermodynamic cycle involves two isobaric and two isosteric steps. Hence, it is convenient to analyze the adsorption isobars in addition to the adsorption isotherms described. From an energetic point of view, we are interested in an adsorption isobar with a single steep step. It is known that small variations in the regeneration conditions can lead to large changes in performance.[46] In this regard, we use pressure control as a mechanism to improve efficiency. The working pressure is based on the onset pressure of the adsorption isotherm at room temperature. The pressure is set for each working pair as the lowest value of pressure that ensures high uptake (immediately after the step in the adsorption isotherm at 298 K). All temperature and pressure conditions of the adsorption isotherms and isobars calculated in this work can be found in the ESI (Table S2†).

Fig. 4c and d show the adsorption isobars of methanol and ethanol in the selected MOFs. These isobars make it possible to determine the regeneration temperature for each working pair under the selected operating conditions. The slope in the desorption isobar is the first indication of the efficiency and performance of a particular working pair. The temperature window for the desorption process is in the range of 300–340 K. Above this range, all structures have released most of the methanol and ethanol load. The maximum adsorption capacity can be related to the pore volume of the adsorbent (Fig. 4e) according to the following trend: MAF-6 > ZIF-8 ≃ ZIF-90 > ZIF-71 > MIL-140C.

The adsorption isotherms calculated for ZIF-8, ZIF-90, and MAF-6 have a steeped behavior, less prominent for ZIF-71 and MIL-140C. This is due to the strong guest–guest interactions of the adsorbates inside the pores, a typical characteristic of hydrophobic materials. These interactions are driven by hydrogen bonds (HB). Fig. 4f shows the average number of hydrogen bonds per molecule (nHB) as a function of pressure for methanol. The values for ethanol can be found in the ESI (Fig. S3a†). At the onset pressure where the adsorption occurs, we found an abrupt increase in the nHB values. At high loading, the nHB in confinement is similar to that in the bulk.[76] We found exceptions for methanol and ethanol in ZIF-71 and ethanol and in MIL-140C. The type of organic ligand is the cause of this situation in ZIF-71. The chlorine atoms are partially located in the large cage, which decreases the degree of hydrophobicity of the structure. This is reflected in the shape of the adsorption isotherm and a lower number of hydrogen bonds within the cavities. MIL-140C is formed by channels

instead of by cages. This particular topology, as well as the size of the structure, implies that the number of hydrogen bonds per ethanol molecule is lower than in the rest of the MOFs.

The structure of the hydrogen bonds changes in confinement, with a competition between molecules of alcohol with one or two HBs (see Fig. S4 in the ESI†), and this is reflected in the guest–guest potential energy (U_{GG}) as a function of external pressure (see Fig. 4g for methanol and ESI, S3b,† for ethanol). All these findings evidence that the adsorption mechanism is driven by the nucleation of the polar molecules through hydrogen bond interactions. This behavior is similar to that found in the adsorption of other polar compounds, such as ammonia, on adsorbents with large cavities.[99]

The energy contribution corresponding to the interaction between methanol and adsorbents is shown in Fig. 4h (for ethanol, see ESI, Fig. S3c†). The affinity between the adsorbates and the internal surface of the framework increases with the host–guest energy. Host–guest interactions generally weaken with loading as preferential adsorption sites fill up and guest–guest interactions become more important. The adsorption onset pressure is strongly related to the host–guest interactions,[100] surface area of the structure, and the kinetic diameter of the adsorbate. In Fig. 4, the infinite dilution regime corresponds to values of pressure below the step in the adsorption isotherm. This regime leads to a reduction in host–guest energy for all the structures except that of MIL-140C. The channel-like structure of this relatively small MOF hinders the nucleation of alcohol molecules and leads to nearly constant values in the host–guest energy for the two adsorbates over the entire pressure range.

The low coverage host–guest energy is approximately twice as high for ZIF-71 and MAF-6 as that for ZIF-8 and ZIF-90, due to the interaction of the first molecules entering the structures with specific binding sites. Methanol and ethanol first interact with the exposed chlorine atoms of the dichloroimidazole link of ZIF-71. As for MAF-6, the alcohol molecules interact with the aromatic rings of the ligand by electrostatic interactions, where the hydroxyl group aligns with the electrostatic field lines pointing towards the center of the ring.[76] After the step in the adsorption isotherm, the host–guest energy decreases to a constant minimum value, while the guest–guest energy reaches the maximum value in the same pressure range. This transition from host–guest to guest–guest interactions points to the nucleation of molecules in hydrophobic MOFs with large pores. Similarly, this energy exchange is the origin of the energy released during the adsorption process, which governs the AHP and ACS devices.

The next stage of our multistep process is the post-processing of the adsorption data using the thermodynamic model. Here, the characteristic curve of adsorption is critical as we can extract a set of relevant quantities from it. As described in the methods, the DP theory relates the adsorption potential (A) and the amount of adsorbed volume (W). One of the limitations is the assumption of the temperature invariance of W. To ensure the applicability of the DP theory, all calculated adsorption isotherms and isobars (see Table S2 of the ESI†) must converge to the same characteristic curve. Fig. 5 shows the characteristic curves of the working pairs from all calculated adsorption curves. The agreement of the different transformations

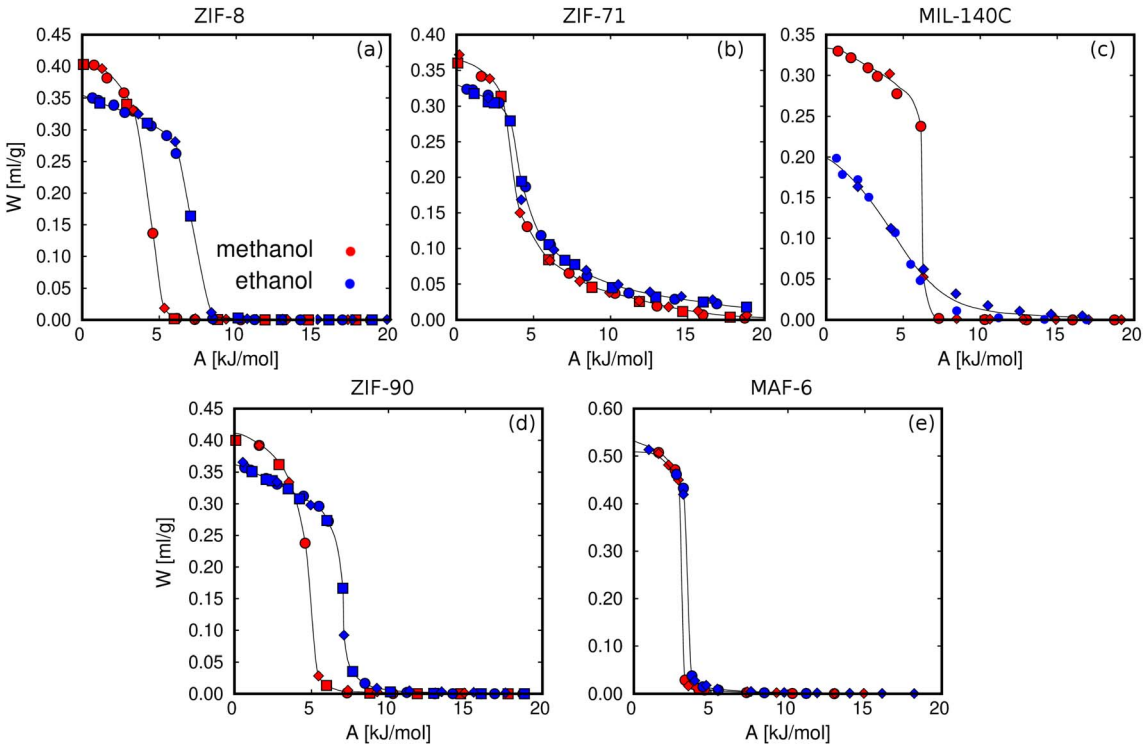

Fig. 5 Characteristic curves determined from the calculated adsorption isotherms and isobars (a) ZIF-8, (b) ZIF-71, (c) MIL-140C, (d) ZIF-90, and (e) MAF-6. The lines correspond to the fitted curves obtained by splines.

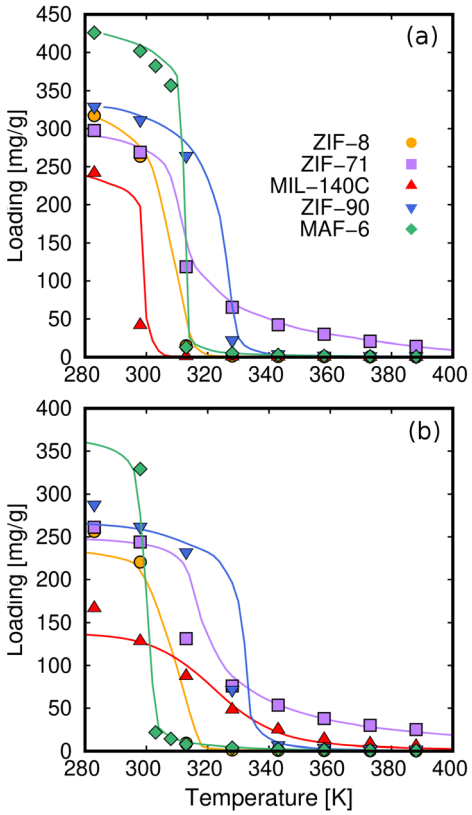

Fig. 6 Adsorption isobars calculated with GCMC simulations (symbols) and from the characteristic curve (lines) of methanol (a) and ethanol (b) in all the adsorbents at the selected working pressures (Table S2†).

indicates the suitability of the DP theory in the systems under study. We can then use the characteristic curve to calculate any adsorption equilibrium relation for a given operating condition since any combination of (p, T) is related *via* the adsorption potential to the working volume and, therefore, to the loading. This interesting property of the characteristic curve can be used to predict adsorption isotherms at different temperatures and adsorption isobars for each working pair. Fig. 6 shows the comparison between the adsorption isobars computed with the GCMC simulations and those predicted from the characteristic curve. The prediction of adsorption isotherms at different temperatures can be found in Fig. S5 of the ESI.† Additionally, Fig. S6† shows the comparison between predicted and computed adsorption isotherms of methanol in ZIF-8, ZIF-90, and ZIF-71 at 353 K, values that were not included to obtain the characteristic curve. The results depicted in Fig. 6, S5, and S6† confirm the predictive power of a single characteristic curve, which can be used to relate the adsorption amount to the operating conditions of the thermodynamic cycle.

To explore the limits of our approach, we computed the relevant properties of AHP and ACS devices. Fig. 7 compares our results for ZIF-8 with previous data from de Lange *et al.*[45] For both working fluids, the characteristic curves are similar in shape and maximum capacity (Fig. 7a). The small differences are due to the choice of density, taken as an approximation by de Lange *et al.*[45] and using Hauer's model. Fig. 7b shows the enthalpy or heat of adsorption as a function of loading. The experimental ΔH was obtained using the Clausius Clapeyron method[101,102] while we are using the Dubinin–Polanyi theory.

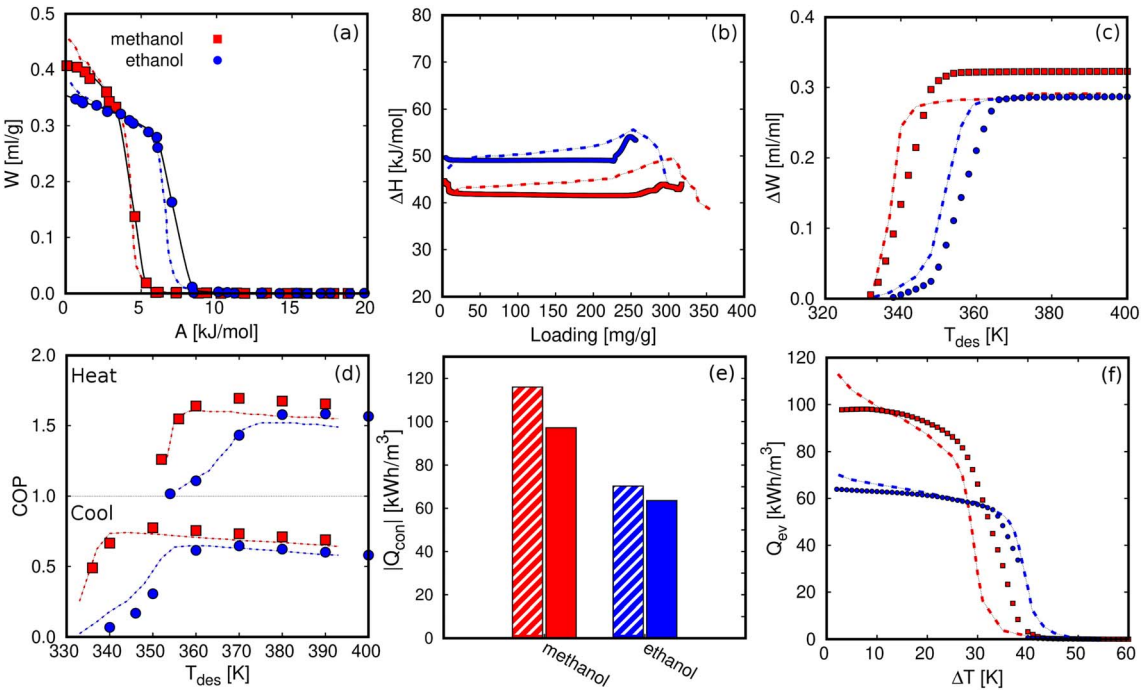

Fig. 7 Comparison between experimental (dashed lines)[45] and computational results (solid symbols) of methanol and ethanol in ZIF-8 for (a) characteristic curves, (b) heat of adsorption as a function of the loading, (c) deliverable capacity (ΔW) as a function of the desorption temperature for refrigeration conditions, $T_{ev} = 278$ K and $T_{con} = 303$ K, (d) COP as a function of the desorption temperature for heating, $T_{ev} = 288$ K and $T_{con} = 318$ K, and cooling, $T_{ev} = 268$ K and $T_{con} = 298$ K, (e) Q_{con} at $T_{con} = 298$ K, and (f) Q_{ev} as a function of the temperature lift ($T_{con} - T_{ev}$), varying T_{ev} with T_{con} and T_{des} set to 298 K and 373 K, respectively.

Fig. 7c exhibits the effect of the desorption temperature on the deliverable capacity under refrigeration conditions. As can be seen, our computed results agree with the experiments. Fig. 7d depicts the COPs for the two working fluids under the operating conditions specified by de Lange *et al.*[45] That is, $T_{ev} = 278$ K and $T_{con} = 303$ K for the ACS and $T_{ev} = 288$ K and $T_{con} = 318$ K for the AHP. The agreement is very good, with only a small deviation due to the ΔH calculation method, saturation pressure estimation, or the adsorbed density model. It is worth noting that de Lange *et al.*[45] approximated the adsorbed density as the liquid density of the fluid, while we used a linear model to describe the temperature dependence of the density of the fluids in confinement. Fig. 7e shows the heat released in the condenser (Q_{con}) at $T_{con} = 298$ K and assuming maximum desorption. Although we used different methods, we found a reasonable agreement. Similarly, Fig. 7f shows the heat released in the evaporator as its temperature differs from the condenser temperature. Based on these results, we can assume that the methodology used could be easily extrapolated to the study of porous materials for AHP and ACS applications.

The COP for the cooling and heating processes using methanol and ethanol allows the comparison of the performance of the adsorbents. In Fig. 7d, we can observe that the COP increases to a maximum value at a certain temperature depending on if the conditions are for heating or cooling applications. After this point, the COP decreases linearly as temperature increases. Methanol generally shows a slightly higher value than ethanol over the entire temperature range. This is a typical representation of the COP values, that is, varying the desorption temperature but setting the temperatures of the evaporator and condenser, respectively. As this property strongly depends on the selection of the operating conditions (see Fig. 1), we can find temperature ranges resulting in low values of COP. However, a single value of the COP could not be an adequate indication of the performance of the material but rather a consequence of the setting of the operating conditions. To clarify this issue, Fig. 8a shows the COP for cooling of ethanol in MAF-6, setting the temperature of the condenser to 288 K, and for two nearby values of the temperature of the evaporator, 273 and 278 K, respectively. We can see that a variation of only five degrees in the operating conditions drastically changes the performance of the working pair, moving from a maximum COP of 0.2 to 0.85. The reason for this drastic change is that the vapor saturation pressure of the adsorbate at the two selected temperatures of the evaporator (273 and 278 K) is in both sides of the step of the adsorption isotherm at the temperature of the condenser (288 K), as shown in Fig. 8b. This confirms that the location of the step of the adsorption isotherms plays an important role in the performance of the AHP devices. A detailed discussion about the ideal location of the step of the isotherms can be found in the literature.[64–66]

The effect shown in Fig. 8a is more noticeable for materials depicting steeped adsorption isotherms or isobars. However, steep adsorption is desired for these applications when complete regeneration of the thermodynamic cycle occurs on a small increase in temperature or pressure lift. To avoid misinterpretation of the performance analysis, we suggest deeply examining each working pair and reducing the number of fixed parameters. To do so, we used the proposed multistep process described in the Methodology section (see Fig. 2), where we iteratively calculated the targeted properties for all possible working temperatures. Thus, instead of having a single relationship between the COP and desorption temperature (Fig. 8a), we obtain a complex data set that shows the evolution of the COP. This is performed by simultaneously varying all the operating temperatures of the thermodynamic cycle.

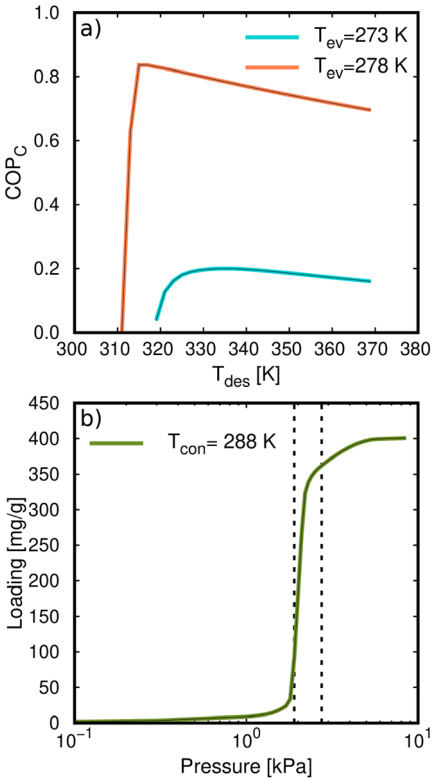

Fig. 8 (a) Coefficient of performance (cooling) of ethanol in MAF-6 as a function of desorption temperature, setting the temperature of the evaporator at 273 K and 278 K, respectively. The temperature of the condenser is set to $T_{con} = 288$ K. (b) Adsorption isotherm of ethanol in MAF-6 at 288 K. The vertical lines represent the vapor saturation pressure of ethanol for the temperatures of the evaporator of 273 K and 278 K, respectively.

Fig. 9 presents the COP for cooling of ethanol in MAF-6 as a function of the temperature of the condenser, evaporator, and desorption. From this data set, we can extract the values of the range of operating conditions that maximize the COP. The optimal desorption temperature must be chosen to ensure complete regeneration of the material, avoiding unnecessary overheating and wasted energy. In this case, the ethanol adsorption in MAF-6 shows a maximum COP for a cooling of 0.84–0.86 at $T_{ev} = 275$–285 K, $T_{con} = 278$–288 K, and $T_{des} = 300$–315 K. However, this theoretical COP value might be impractical in real applications since the optimal temperatures that maximize the COP are out of the range of the operational conditions for ACS applications. In a more realistic scenario, one can set the operational temperatures between minimum and

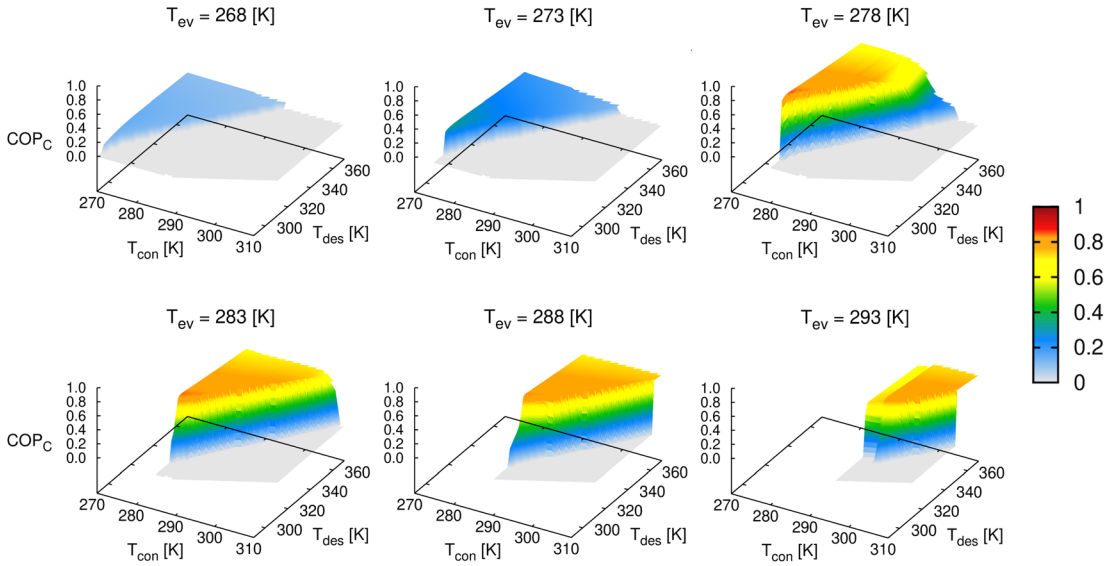

Fig. 9 Evolution of the coefficient of performance (cooling) of ethanol in MAF-6 by varying the operating temperature of the thermodynamic cycle (see Fig. 1).

maximum boundaries. In this situation, the COP for cooling using ethanol and MAF-6 working pairs shows maximum values between 0.80 and 0.82 at $T_{ev} = 285$–290 K, $T_{con} = 298$–303 K, and $T_{des} = 330$–340 K.

To compare the results obtained in the five MOFs, Fig. 10 shows the COP for cooling, setting the temperature of the evaporator to 278 K. This temperature is within the range of operating conditions for cooling applications, and all working pairs reach the optimum level of COP values. In general, methanol performs better than ethanol for cooling applications, which could be due to better molecular packaging leading to higher adsorption capacity. The superior performance of MAF-6 compared to the other adsorbents is remarkable. The high adsorption capacity and especially steeped adsorption behavior make this MOF outperform the rest under study for AHP and ACS applications.

The heat energy transferred to the condenser (Q_{con}) that we show in Fig. 7e is another relevant property. The values obtained for the five MOFs for both methanol and ethanol are shown in Fig. 11a and b. The volumetric energy released in the condenser shows similar values for heating and cooling applications and shows that methanol releases more energy than ethanol. Again, the exception to the rule is the value of ethanol in MAF-6 for cooling applications for the same reasons as for COP. We obtained the Q_{con} assuming a complete regeneration of the cycle, *i.e.*, maximum desorption of the adsorbates. This means that the only temperatures that affect the calculation of Q_{con} are those of the evaporator and condenser. To get a broader overview of the variation of Q_{con} of methanol and ethanol with operating temperatures, we plot Q_{con} as a function of T_{con} and T_{ev} in Fig. 11c and d. In addition, Fig. S7–S10† show a comparison of the Q_{con} for both working fluids in all the adsorbents. The figures are represented in volumetric (kW h m^{-3}) and gravimetric (kJ kg^{-1}) units to show the effect of the framework

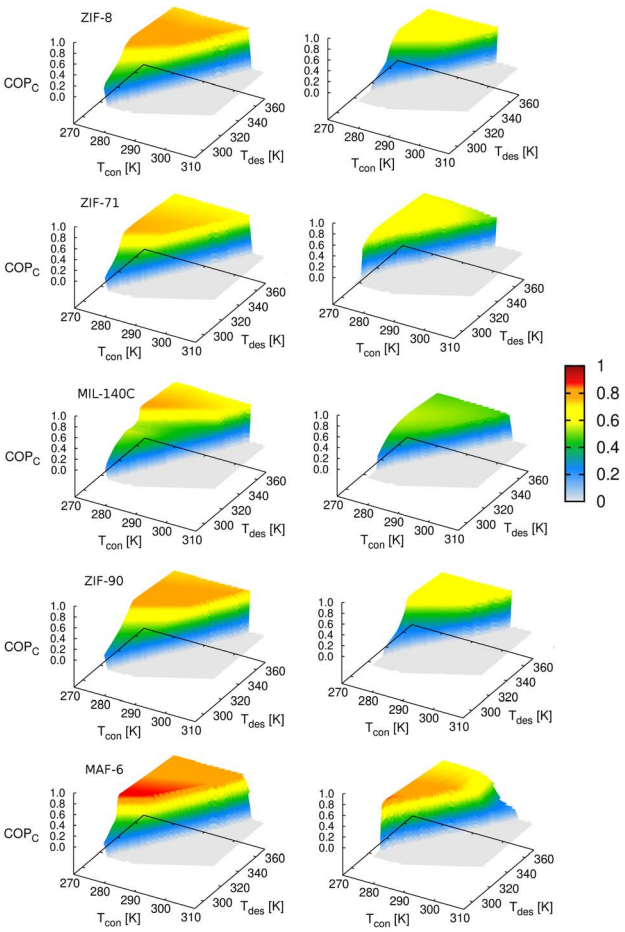

Fig. 10 Coefficient of performance (cooling) of methanol (left column) and ethanol (right column) by varying the operating temperature of the thermodynamic cycle (see Fig. 1). The temperature of the evaporator is set to $T_{ev} = 278$ K.

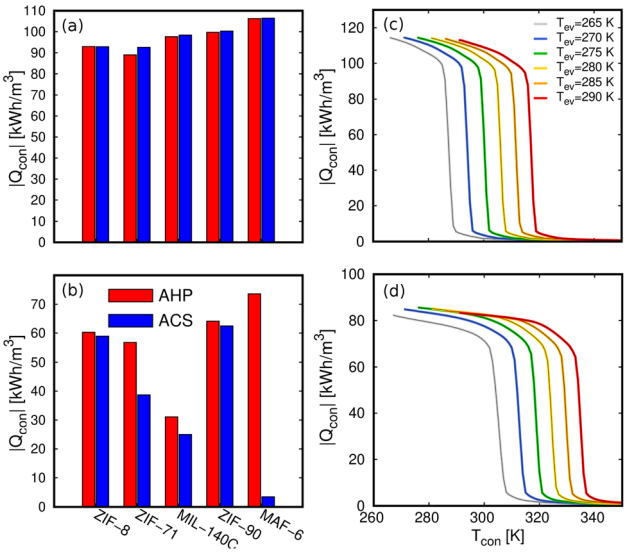

Fig. 11 Volumetric heat energy transferred to the condenser per unit of volume of the MOF using (a) methanol and (b) ethanol for the AHP (red) at $T_{ev} = 273$ K and $T_{con} = 288$ K and ACS (blue) at $T_{ev} = 283$ K and $T_{con} = 298$ K. Volumetric heat energy transferred to the condenser per unit of volume of the MOF using (c) methanol and (d) ethanol in MAF-6 with variation of the temperature of the evaporator assuming full desorption.

density on the energy released by the adsorbent. From all the data, we selected MAF-6 as the reference MOF because it was the best performing structure. In line with the adsorption isotherms and isobars, MAF-6 shows a pronounced Q_{con}, suggesting the importance of selecting the working conditions. After the step, all curves converge to a similar maximum Q_{con} value, which is the optimal value for each working pair.

In line with the previous results, we can use the multistep approach to analyze other relevant properties for heating or cooling applications as a function of the desired conditions. These properties are, for example, the specific heating (SHE) or cooling effect (SCE), the working volume or deliverable capacity (ΔW), or the heat released or required by the evaporator (Q_{ev}). The values for these properties obtained in MAF-6 for methanol and ethanol are shown in Fig. 12. The values obtained for the other MOFs can be found in the ESI (Fig. S11–S13†). As mentioned above, methanol performs better than ethanol in all the properties studied here due to its optimal molecular packing. We also found that all properties are very sensitive to the operating conditions, moving from low to high values in a minimal interval. Because of the number of variables defining the thermodynamic cycle, these drastic changes cannot be predicted from the behavior of the adsorption isotherms or isobars. Under these circumstances, our multistep method that covers all the conditions simultaneously proves to be an efficient technique for analyzing the performance of adsorption-based energy storage devices. For example, the complex landscape of the SHE and SCE of methanol and ethanol in MAF-6 (see Fig. 12) can lead to very different values when setting some of the operational temperatures. This behavior is similar to that in the COP shown in Fig. 8. In a simpler comparison, when

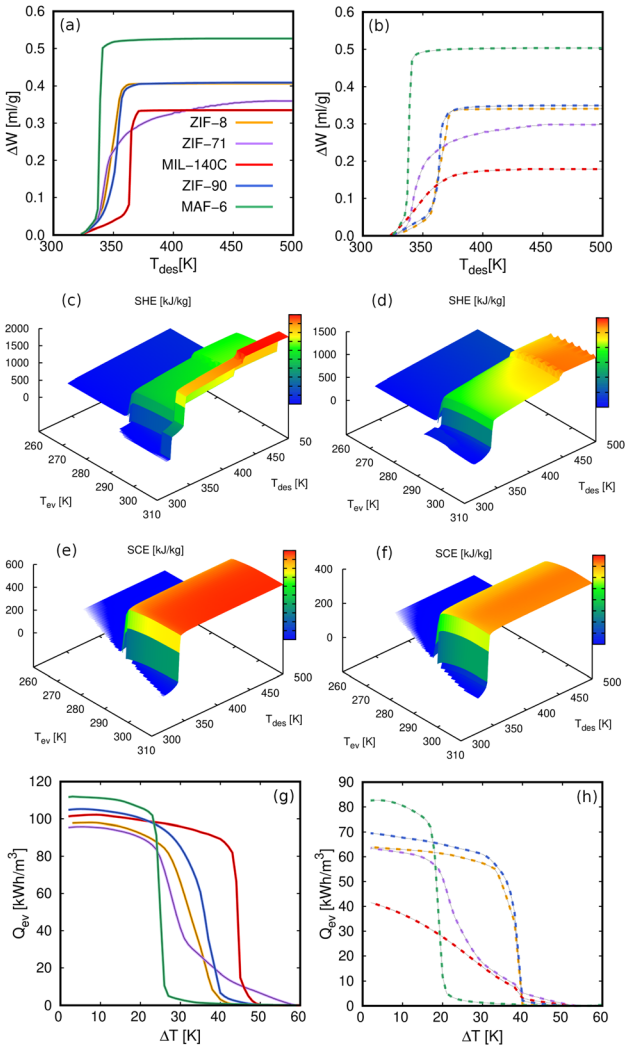

Fig. 12 Deliverable capacity for (a) methanol and (b) ethanol as a function of the desorption temperature for $T_{ev} = 300$ K and $T_{con} = 310$ K. The SHE and SCE of (c and e) methanol and (d and f) ethanol in MAF-6 at $T_{con} = 313$ K. Q_{ev} as a function of temperature lift ($T_{con} - T_{ev}$), for (g) methanol and (h) ethanol varying T_{ev} with T_{con} and T_{des} set to 298 K and 373 K, respectively.

working conditions are set to specific values, MAF-6 did not appear as the best performing adsorbent. However, among all MOFs, MAF-6 shows the highest values for all the analyzed quantities. In general, all working pairs studied here show good performance for AHP and ACS applications. However, considering the energy release in the condenser and evaporator, the coefficient of performance, and the highest adsorption and release capacity, the best choice would be MAF-6.

4 Conclusions

We shed light on the mechanisms governing adsorption-driven heat pumps for heating and cooling applications using MOFs and light alcohols. To this aim, we evaluated the performance of five MOFs using methanol and ethanol as working fluids. Adsorption isotherms and isobars, energetic interactions

between molecules and adsorbents, and nucleation of the fluids in confinement were calculated from simulations. Adsorption data were processed using mathematical modeling based on the Dubinin–Polanyi theory of adsorption and a thermodynamic model to describe relevant properties for heating and cooling applications. Finally, we proposed a multistep approach to analyze the relationships between performance and operating conditions, which allows the optimal working conditions for each adsorbent–fluid pair to be described.

All MOFs selected, combined with methanol, show high performance for AHP and ACS applications. The performance coefficients were above 0.8 for cooling and 1.8 for heating. The energy released to the condenser was above 90 kW h m^{-3}. The yield associated with ethanol adsorption is lower than that for methanol but still significant for MAF-6. This MOF outperforms the other adsorbents studied here for AHP and ACS applications under a wide range of operating conditions. It exhibits a COP above 0.9 and 1.9 for cooling and heating, respectively, and Q_{con} and Q_{ev} about 115 kW h m^{-3} for methanol. With a pore size of about 18 Å and relatively low density, the hydrophobic MAF-6 exhibits large pore volume and surface area, resulting in a steeped isotherm and large adsorption capacity for light alcohols.

Overall, the multistep process proposed here seems to be an efficient tool for analyzing the performance of working pairs for heating and cooling applications. We have proven the importance of removing constraints for applying the thermodynamic model. Establishing or assuming fixed values of certain operating temperatures could lead to misinterpretation of the performance of the working pairs. This is particularly remarkable for systems showing steeped isotherms, which at the same time are desired for these applications. An increase in the temperature by a few degrees could decrease the performance of a working pair by 80%. Another advantage of the proposed approach is that it only needs an adsorption isobar or isotherm as the input. This approach can be combined with simulation data or experimental measurements since we employed mathematical modeling to post-process the adsorption data. We show that we can simultaneously describe experimental results from the literature with high accuracy and predict various properties involved in heating and cooling applications.

Author contributions

R. M. M.-C. and A. L.-T. contributed equally to this work. J. M. V.-L. organized and supervised the project. All authors provided feedback on the interpretation of the results and data analysis, and helped in writing and revising the manuscript.

Conflicts of interest

There are no conflicts to declare.

Acknowledgements

This work was supported by Ministerio de Ciencia, Innovación y Universidades (CTQ2017-95-173-EXP). A. L.-T. and S. C. acknowledge funding by the Irène Curie Fellowship program of the Eindhoven University of Technology, and J. M. V.-L. acknowledges the APSE department of TU/e for funding support and computing resources. We thank C3UPO for the HPC support.

References

1 S. Sayadi, G. Tsatsaronis, T. Morosuk, M. Baranski, R. Sangi and D. Muller, *J. Cleaner Prod.*, 2019, **241**, 118277.
2 L. Pérez-Lombard, J. Ortiz and C. Pout, *Energy Build.*, 2008, **40**, 394–398.
3 M. Isaac and D. P. van Vuuren, *Energy Policy*, 2009, **37**, 507–521.
4 X. Hu, M. Cai, S. Yang and S. A. Sejas, *Sci. China: Earth Sci.*, 2018, **61**, 1491–1509.
5 F. Joos, *Nature*, 2015, **522**, 295.
6 B. Govindasamy, S. Thompson, A. Mirin, M. Wickett, K. Caldeira and C. Delire, *Tellus B*, 2005, **57**, 153–163.
7 C. C. Hay, E. Morrow, R. E. Kopp and J. X. Mitrovica, *Nature*, 2015, **517**, 481–484.
8 D. Liu, X. Guo and B. Xiao, *Sci. Total Environ.*, 2019, **661**, 750–766.
9 D. Coumou, A. Robinson and S. Rahmstorf, *Clim. Change*, 2013, **118**, 771–782.
10 A. Elsheikh, S. Sharshir, M. E. Mostafa, F. Essa and M. K. Ahmed Ali, *Renewable Sustainable Energy Rev.*, 2018, **82**, 3483–3502.
11 D. Proszak-Miąsik, E. Rybak-Wilusz and S. Rabczak, *J. Ecol. Eng.*, 2020, **21**, 1–7.
12 A. Sharma, V. Tyagi, C. Chen and D. Buddhi, *Renewable Sustainable Energy Rev.*, 2009, **13**, 318–345.
13 A. Kumar, O. Prakash and A. K. Kaviti, *Renewable Sustainable Energy Rev.*, 2017, **77**, 890–898.
14 N. Kannan and D. Vakeesan, *Renewable Sustainable Energy Rev.*, 2016, **62**, 1092–1105.
15 K. Wojdyga, *Energy Build.*, 2008, **40**, 2009–2014.
16 K. Chua, S. Chou and W. Yang, *Appl. Energy*, 2010, **87**, 3611–3624.
17 B. Kuyper, D. Say, C. Labuschagne, T. Lesch, W. R. Joubert, D. Martin, D. Young, M. A. H. Khan, M. Rigby, A. L. Ganesan, M. F. Lunt, C. O'Dowd, A. J. Manning, S. O'Doherty, M. T. Davies-Coleman and D. E. Shallcross, *Environ. Sci. Technol.*, 2019, **53**, 8967–8975.
18 S. Wongwises and N. Chimres, *Energy Convers. Manage.*, 2005, **46**, 85–100.
19 L. Hu, S. A. Montzka, S. J. Lehman, D. S. Godwin, B. R. Miller, A. E. Andrews, K. Thoning, J. B. Miller, C. Sweeney, C. Siso, J. W. Elkins, B. D. Hall, D. J. Mondeel, D. Nance, T. Nehrkorn, M. Mountain, M. L. Fischer, S. C. Biraud, H. Chen and P. P. Tans, *Geophys. Res. Lett.*, 2017, **44**, 8075–8083.
20 M. Teker, M. İmamoğlu and Ö. Saltabaş, *Turk. J. Chem.*, 1999, **23**, 185–192.
21 G. Cacciola, G. Restuccia and L. Mercadante, *Carbon*, 1995, **33**, 1205–1210.
22 R. E. Critoph, *Carbon*, 1989, **27**, 63–70.

23 L. Wang, J. Wu, R. Wang, Y. Xu, S. Wang and X. Li, *Appl. Therm. Eng.*, 2003, **23**, 1605–1617.
24 T. Kohler and K. Muller, *Energy Sci. Eng.*, 2017, **5**, 21–29.
25 L. Trager, J. Glasel, M. Scherle, J. Hartmann, U. Nieken and B. J. M. Etzold, *Chem. Eng. Technol.*, 2020, **43**, 1876–1883.
26 Z. Tamainot-Telto and R. Critoph, *Appl. Therm. Eng.*, 2001, **21**, 37–52.
27 I. I. El-Sharkawy, A. Pal, T. Miyazaki, B. B. Saha and S. Koyama, *Appl. Therm. Eng.*, 2016, **98**, 1214–1220.
28 A. A. Askalany, S. K. Henninger, M. Ghazy and B. B. Saha, *Appl. Therm. Eng.*, 2017, **110**, 695–702.
29 A. Capri, A. Frazzica and L. Calabrese, *Coatings*, 2020, **10**, 855.
30 R. E. Critoph and Y. Zhong, *Proc. Inst. Mech. Eng., Part E*, 2005, **219**, 285–300.
31 A. Freni, G. Maggio, A. Sapienza, A. Frazzica, G. Restuccia and S. Vasta, *Appl. Therm. Eng.*, 2016, **104**, 85–95.
32 L. Calabrese, V. Brancato, L. Bonaccorsi, A. Frazzica, A. Capri, A. Freni and E. Proverbio, *Appl. Therm. Eng.*, 2017, **116**, 364–371.
33 X. Zheng, R. Wang, T. Ge and L. Hu, *Energy*, 2015, **93**, 88–94.
34 A. Freni, L. Bonaccorsi, L. Calabrese, A. Capri, A. Frazzica and A. Sapienza, *Appl. Therm. Eng.*, 2015, **82**, 1–7.
35 A. Atakan, G. Fueldner, G. Munz, S. Henninger and M. Tatlier, *Appl. Therm. Eng.*, 2013, **58**, 273–280.
36 M. Tatlier, *Heat Mass Transfer*, 2021, **57**, 975–984.
37 R. M. Madero-Castro, A. Luna-Triguero, A. Sławek, J. M. Vicent-Luna and S. Calero, *ACS Sustain. Chem. Eng.*, 2023, **11**, 4317–4328.
38 M. F. de Lange, K. J. F. M. Verouden, T. J. H. Vlugt, J. Gascon and F. Kapteijn, *Chem. Rev.*, 2015, **115**, 12205–12250.
39 S. K. Henninger, S.-J. Ernst, L. Gordeeva, P. Bendix, D. Fröhlich, A. D. Grekova, L. Bonaccorsi, Y. Aristov and J. Jaenchen, *Renewable Energy*, 2017, **110**, 59–68.
40 H. Kummer, F. Jeremias, A. Warlo, G. Füldner, D. Fröhlich, C. Janiak, R. Gläser and S. K. Henninger, *Ind. Eng. Chem. Res.*, 2017, **56**, 8393–8398.
41 F. Jeremias, D. Fröhlich, C. Janiak and S. K. Henninger, *RSC Adv.*, 2014, **4**, 24073–24082.
42 D. M. Steinert, S.-J. Ernst, S. K. Henninger and C. Janiak, *Eur. J. Inorg. Chem.*, 2020, **2020**, 4502–4515.
43 J. M. Pinheiro, S. Salústio, V. Geraldes, A. A. Valente and C. M. Silva, *Appl. Therm. Eng.*, 2020, **178**, 115498.
44 A. Pal, K. Thu, S. Mitra, I. I. El-Sharkawy, B. B. Saha, H.-S. Kil, S.-H. Yoon and J. Miyawaki, *Int. J. Heat Mass Transfer*, 2017, **110**, 7–19.
45 M. F. de Lange, B. L. van Velzen, C. P. Ottevanger, K. J. F. M. Verouden, L.-C. Lin, T. J. H. Vlugt, J. Gascon and F. Kapteijn, *Langmuir*, 2015, **31**, 12783–12796.
46 W. Li, X. Xia, M. Cao and S. Li, *J. Mater. Chem. A*, 2019, **7**, 7470–7479.
47 M. Erdos, M. F. de Lange, F. Kapteijn, O. A. Moultos and T. J. H. Vlugt, *ACS Appl. Mater. Interfaces*, 2018, **10**, 27074–27087.
48 F. Jeremias, D. Frohlich, C. Janiak and S. K. Henninger, *New J. Chem.*, 2014, **38**, 1846–1852.
49 S. Kayal, S. Baichuan and B. B. Saha, *Int. J. Heat Mass Transfer*, 2016, **92**, 1120–1127.
50 Cambridge Crystallographic Data Centre, **https://www.ccdc.cam.ac.uk**.
51 K. Zhang, R. P. Lively, M. E. Dose, A. J. Brown, C. Zhang, J. Chung, S. Nair, W. J. Koros and R. R. Chance, *Chem. Commun.*, 2013, **49**, 3245–3247.
52 C.-T. He, L. Jiang, Z.-M. Ye, R. Krishna, Z.-S. Zhong, P.-Q. Liao, J. Xu, G. Ouyang, J.-P. Zhang and X.-M. Chen, *J. Am. Chem. Soc.*, 2015, **137**, 7217–7223.
53 C. M. Keinath, S. Garimella and M. A. Garrabrant, *Int. J. Refrig.*, 2017, **83**, 39–50.
54 A. Luna-Triguero, A. Sławek, H. P. Huinink, T. J. H. Vlugt, A. Poursaeidesfahani, J. M. Vicent-Luna and S. Calero, *ACS Appl. Nano Mater.*, 2019, **2**, 3050–3059.
55 J. R. Álvarez, E. Sánchez-González, E. Pérez, E. Schneider-Revueltas, A. Martínez, A. Tejeda-Cruz, A. Islas-Jácome, E. González-Zamora and I. A. Ibarra, *Dalton Trans.*, 2017, **46**, 9192–9200.
56 R. M. Madero-Castro, J. M. Vicent-Luna, X. Peng and S. Calero, *ACS Sustain. Chem. Eng.*, 2022, **10**, 6509–6520.
57 E. E. Sann, Y. Pan, Z. Gao, S. Zhan and F. Xia, *Sep. Purif. Technol.*, 2018, **206**, 186–191.
58 S. Calero and P. Gómez-Álvarez, *J. Phys. Chem. C*, 2015, **119**, 23774–23780.
59 B. Van de Voorde, D. Damasceno Borges, F. Vermoortele, R. Wouters, B. Bozbiyik, J. Denayer, F. Taulelle, C. Martineau, C. Serre, G. Maurin and D. De Vos, *ChemSusChem*, 2015, **8**, 3159–3166.
60 C.-T. He, L. Jiang, Z.-M. Ye, R. Krishna, Z.-S. Zhong, P.-Q. Liao, J. Xu, G. Ouyang, J.-P. Zhang and X.-M. Chen, *J. Am. Chem. Soc.*, 2015, **137**, 7217–7223.
61 R. Pacheco and C. Silva, *Energies*, 2019, **12**, 2535.
62 W. Li, X. Xia and S. Li, *ACS Appl. Mater. Interfaces*, 2020, **12**, 3265–3273.
63 X. Xia, Z. Liu and S. Li, *Appl. Therm. Eng.*, 2020, **176**, 115442.
64 M. H. Bagheri and S. N. Schiffres, *Langmuir*, 2018, **34**, 1908–1915.
65 Y. Jiang, M. H. Bagheri, R. T. Loibl and S. N. Schiffres, *Appl. Therm. Eng.*, 2019, **160**, 113906.
66 W. Li, Z. Liu and S. Li, *Therm. Sci. Eng. Prog.*, 2021, **25**, 101033.
67 K. S. Park, Z. Ni, A. P. Côté, J. Y. Choi, R. Huang, F. J. Uribe-Romo, H. K. Chae, M. O'Keeffe and O. M. Yaghi, *Proc. Natl. Acad. Sci. U. S. A.*, 2006, **103**, 10186–10191.
68 F.-K. Shieh, S.-C. Wang, S.-Y. Leo and K. C. Wu, *Chem.–Eur. J.*, 2013, **19**, 11139–11142.
69 S. Liu, G. Liu, X. Zhao and W. Jin, *J. Membr. Sci.*, 2013, **446**, 181–188.
70 V. Guillerm, F. Ragon, M. Dan-Hardi, T. Devic, M. Vishnuvarthan, B. Campo, A. Vimont, G. Clet, Q. Yang, G. Maurin, G. Férey, A. Vittadini, S. Gross and C. Serre, *Angew Chem., Int. Ed. Engl.*, 2012, **51**, 9267–9271.
71 D. Dubbeldam, S. Calero, D. E. Ellis and R. Q. Snurr, *Mol. Simul.*, 2016, **42**, 81–101.
72 D. Dubbeldam, A. Torres-Knoop and K. S. Walton, *Mol. Simul.*, 2013, **39**, 1253–1292.

73 D. Boda and D. Henderson, *Mol. Phys.*, 2008, **106**, 2367–2370.
74 T. Darden, D. York and L. Pedersen, *J. Chem. Phys.*, 1993, **98**, 10089–10092.
75 J. M. Stubbs, J. J. Potoff and J. I. Siepmann, *J. Phys. Chem. B*, 2004, **108**, 17596–17605.
76 R. M. Madero-Castro, J. M. Vicent-Luna and S. Calero, *J. Phys. Chem. C*, 2019, **123**, 23987–23994.
77 K. Zhang, L. Zhang and J. Jiang, *J. Phys. Chem. C*, 2013, **117**, 25628–25635.
78 R. Banerjee, A. Phan, B. Wang, C. Knobler, H. Furukawa, M. O'Keeffe and O. M. Yaghi, *Science*, 2008, **319**, 939–943.
79 W. Morris, C. J. Doonan, H. Furukawa, R. Banerjee and O. M. Yaghi, *J. Am. Chem. Soc.*, 2008, **130**, 12626–12627.
80 X.-C. Huang, Y.-Y. Lin, J.-P. Zhang and X.-M. Chen, *Angew Chem. Int. Ed. Engl.*, 2006, **45**, 1557–1559.
81 S. L. Mayo, B. D. Olafson and W. A. Goddard, *J. Phys. Chem.*, 1990, **94**, 8897–8909.
82 A. K. Rappe, C. J. Casewit, K. S. Colwell, W. A. I. Goddard and W. M. Skiff, *J. Am. Chem. Soc.*, 1992, **114**, 10024–10035.
83 D. Ongari, P. G. Boyd, O. Kadioglu, A. K. Mace, S. Keskin and B. Smit, *J. Chem. Theory Comput.*, 2019, **15**, 382–401.
84 J. J. Gutierrez-Sevillano, S. Calero, C. O. Ania, J. B. Parra, F. Kapteijn, J. Gascon and S. Hamad, *J. Phys. Chem. C*, 2013, **117**, 466–471.
85 V. Majer and V. Svoboda, *Enthalpies of Vaporization of Organic Compounds: a Critical Review and Data Compilation*, 1986.
86 M. M. Dubinin, *Chem. Rev.*, 1960, **60**, 235–241.
87 M. M. Dubinin, *Bull. Acad. Sci. USSR, Div. Chem. Sci.*, 1960, **9**, 1072–1078.
88 M. Polanyi, *Science*, 1963, **141**, 1010–1013.
89 C. Lehmann, S. Beckert, T. Nonnen, J. Möllmer, R. Gläser, O. Kolditz and T. Nagel, *Energy Procedia*, 2017, **105**, 4334–4339.
90 C. Lehmann, S. Beckert, R. Gläser, O. Kolditz and T. Nagel, *Appl. Energy*, 2017, **185**, 1965–1970.
91 D.-Y. Peng and D. B. Robinson, *Ind. Eng. Chem. Fundam.*, 1976, **15**, 59–64.
92 T. Nagel, S. Beckert, N. Böttcher, R. Gläser and O. Kolditz, *Energy Procedia*, 2015, **75**, 2106–2112.
93 B. na González, N. Calvar, E. Gómez and A. Domínguez, *J. Chem. Thermodyn.*, 2007, **39**, 1578–1588.
94 B. Bering, M. Dubinin and V. Serpinsky, *J. Colloid Interface Sci.*, 1966, **21**, 378–393.
95 A. Ristić, F. Fischer, A. Hauer and N. Zabukovec Logar, *J. Mater. Chem. A*, 2018, **6**, 11521–11530.
96 X. Peng, J. M. Vicent-Luna, S. K. Jain, Q. Jin and J. K. Singh, *ACS Appl. Nano Mater.*, 2019, **2**, 7103–7113.
97 Y. Tang, D. Dubbeldam and S. Tanase, *ACS Appl. Mater. Interfaces*, 2019, **11**, 41383–41393.
98 Y. I. Aristov, *Appl. Therm. Eng.*, 2013, **50**, 1610–1618.
99 I. Matito-Martos, A. Martin-Calvo, C. Ania, J. Parra, J. Vicent-Luna and S. Calero, *Chem. Eng. J.*, 2020, **387**, 124062.
100 J.-R. Li, R. J. Kuppler and H.-C. Zhou, *Chem. Soc. Rev.*, 2009, **38**, 1477–1504.
101 H. Pan, J. A. Ritter and P. B. Balbuena, *Langmuir*, 1998, **14**, 6323–6327.
102 R. T. Cimino, P. Kowalczyk, P. I. Ravikovitch and A. V. Neimark, *Langmuir*, 2017, **33**, 1769–1779.